Nanoscale Research Letters

NANO EXPRESS

Open Access

# Highly Sensitive and Selective Sensing of $H_2S$ Gas Using Precipitation and Impregnation-Made $CuO/SnO_2$ Thick Films

Pimpan Leangtanom[1], Anurat Wisitsoraat[4], Kata Jaruwongrangsee[5], Narong Chanlek[6], Adisorn Tuantranont[4], Sukon Phanichphant[7] and Viruntachar Kruefu[1,2,3*]

## Abstract

In this work, CuO-loaded tetragonal $SnO_2$ nanoparticles ($CuO/SnO_2$ NPs) were synthesized using precipitation/impregnation methods with varying Cu contents of 0–25 wt% and characterized for $H_2S$ detection. The material phase, morphology, chemical composition, and specific surface area of NPs were evaluated using X-ray diffraction, transmission electron microscopy, scanning electron microscopy, energy-dispersive X-ray spectroscopy, X-ray photoelectron spectroscopy, and Brunauer–Emmett–Teller analysis. From gas-sensing data, the $H_2S$ responses of $SnO_2$ NPs were greatly enhanced by CuO loading particularly at the optimal Cu content of 20 wt%. The 20 wt% $CuO/SnO_2$ sensor showed an excellent response of $1.36 \times 10^5$ toward 10 ppm $H_2S$ and high $H_2S$ selectivity against $H_2$, $SO_2$, $CH_4$, and $C_2H_2$ at a low optimum working temperature of 200 °C. In addition, the sensor provided fast response and a low detection limit of less than 0.15 ppm. The CuO–$SnO_2$ sensor could therefore be a potential candidate for $H_2S$ detection in environmental applications.

**Keywords:** Precipitation/impregnation, $CuO/SnO_2$ thick films, Gas sensor, Sensing mechanism, Hydrogen sulfide

## Background

Hydrogen sulfide ($H_2S$) is a highly toxic gas widely produced from several sources, such as manure fermentation plants, wastewater treatment systems, petroleum refineries, landfill sites, textile factories, stagnant water wells, extruded rubber industries, and other similar industrial facilities. $H_2S$ can be adsorbed through human lungs, gastrointestinal regions, and normal skin. Its funky odor will freeze the sense of smell leading to immediate paralysis and mortality when its concentration exceeds its threshold limit value (TLV) of 10 ppm [1]. Therefore, it is compelling to develop an effective and low-cost gas sensor that can detect $H_2S$ at sub-ppm concentrations with high response, short response time, high selectivity and good stability.

Semiconducting metal oxides, such as zinc oxide (ZnO), tin dioxide ($SnO_2$), titanium dioxide ($TiO_2$) and nickel oxide (NiO), have been extensively studied for various gas-sensing applications [2–6]. Among them, tin dioxide ($SnO_2$) has been regarded as the most promising n-type metal oxide gas-sensing material due to its low cost, diverse gas response, ease of doping, high chemical stability, and wide range of working temperature from 100 to 600 °C [7–9]. In particular, it has been reported as one of the most attractive candidates for $H_2S$ detection after the modification by doping with metallic dopants [10–18], loading with metal oxide nanoparticles [19–27], and forming nanocomposites with different metal oxide semiconductors [28, 29]. However, the $H_2S$-sensing performances of $SnO_2$ still need further improvements.

Copper Oxide (CuO) is a functional p-type metal oxide semiconductor with a moderate energy gap of

*Correspondence: v_viruntachar@hotmail.com
[1] Applied Chemistry Program, Faculty of Science, Maejo University, Chiang Mai 50290, Thailand
Full list of author information is available at the end of the article

1.2–2.0 eV, remarkable sensitivity and selectivity toward $H_2S$. CuO-loaded $SnO_2$ gas sensors have been extensively characterized toward $H_2S$ as presented in Table 1. CuO dopants provides relatively high enhancement of $H_2S$ response and selectivity for $SnO_2$ sensors [19–27]. The $H_2S$-sensing performances also depend substantially on the synthesis method and the form of metal oxide materials. From the table, recent reports CuO/$SnO_2$ sensors are mostly in thick-film and thin-film forms, which offer similarly competitive $H_2S$-sensing performances depending on synthesis method and preparation parameters. Between them, thick-film sensors are more preferred in practical applications due to their much lower production cost. Hence, it is compelling to investigate the $H_2S$-sensing properties of thick-film CuO/$SnO_2$ materials prepared by other advanced techniques.

Precipitation and impregnation are attractive methods for production of thick-film nanocomposite materials because of ability to form diverse nanostructures, low processing temperature, and low cost. Some CuO-loaded $SnO_2$ nanomaterials synthesized by precipitation with $NH_3$ precipitant and impregnation were studied for $H_2S$ gas-sensing. However, the reported results still offered only modest response at high $H_2S$ concentrations due possibly to large particle sizes [28]. Herein, precipitated $SnO_2$ nanoparticles (NPs) were prepared using NaOH as a precipitant and impregnated with CuO at over a wide range of Cu contents to attain small nanoparticles and large responses at relatively low $H_2S$ concentrations. Thick-film sensors were fabricated by spin coating powder paste of synthesized CuO/$SnO_2$ nanoparticles and the effects of CuO loading level on $H_2S$-sensing properties were explained based on CuO/$SnO_2$ heterojunctions.

## Methods

### Synthesis and Characterization of Nanoparticles

All chemicals with analytical grade were used directly without additional purification. Tin (IV) chloride pentahydrate ($SnCl_4{\cdot}5H_2O$) as a tin source was dissolved in deionized (DI) water under constant stirring to obtain the 0.1 M aqueous solution. An appropriate volume of 0.1 M sodium hydroxide (NaOH) aqueous solution was slowly dropped onto the $SnCl_4$·solution under vigorous stirring until white slurry appeared at the pH of 11. The slurry was washed thoroughly with DI water several times under centrifugation to remove chloride residues from the precipitate. The resulting precipitate was subsequently dried at 80 °C for 10 h in an oven and the obtained particles were calcined for 2 h at 600 °C at a heating rate of 10 °C/min. To impregnate CuO onto $SnO_2$ nanoparticles, 0.872 g of copper (II) acetate hydrate (98%; Aldrich) was dissolved in 30 mL of ethanol under

**Table 1** A summary of $H_2S$ response of metal-loaded $SnO_2$ and CuO/$SnO_2$ nanomaterials prepared by various methods

| Materials | Form | Technical used | Gas conc. (ppm)/ Temp (°C) | $H_2S$ Response | Refs |
|---|---|---|---|---|---|
| 3.0 mol% Ag–$SnO_2$ | Thick film | Spray pyrolysis | 450/100 | 1.38 | [10] |
| 0.1 wt% V–$SnO_2$ | Thick film | Flame spray pyrolysis and spin coating | 10/350 | $2.27 \times 10^3$ | [11] |
| 0.5 wt% Mo–$SnO_2$ | Thick film | Flame spray pyrolysis and spin coating | 10/250 | ≈105 | [12] |
| Sb–$SnO_2$ nanoribbons | Thin film | Thermal evaporation | 100/150 | ≈55 | [13] |
| 0.64 at% Fe–$SnO_2$ | Thin film | Rheotaxial grown and Thermal oxidation | 10/225 | 14.5 | [14] |
| Cu-doped $SnO_2$ | Thick film | Ultrasonic spray pyrolysis | 95.9/100 | $7.24 \times 10^3$ | [15] |
| 2mol% Cu–$SnO_2$ | Thick film | Hydrothermal and drip coating | 300/300 | 40 | [16] |
| Cu–$SnO_2$ nanowires | Thin film | Thermal evaporation | 10/150 | $5 \times 10^5$ | [17] |
| 1 at% Cu–$SnO_2$ | Thick film | Electrostatic sprayed | 10/100 | $2.5 \times 10^3$ | [18] |
| $SnO_2$/CuO islands | Thin film | Sputtering | 5/250 | 128 | [19] |
| CuO-loaded $SnO_2$ | Thick film | Ultrasonic spray pyrolysis | 1/300 | 22.4 | [20] |
| CuO/$SnO_2$ | Thin film | Chemical vapour deposition | 10/250 | 26.3 | [21] |
| 3 vol% CuO–$SnO_2$ | Thin film | Pulsed laser deposition | 20/140 | $2.7 \times 10^4$ | [22] |
| CuO-loaded $SnO_2$ | Thin film | Electrospinning | 10/300 | $1.98 \times 10^4$ | [23] |
| 5 mol% CuO/$SnO_2$ | Thin film | Co-dissolution and electrospinning | 1/200 | ≈23 | [24] |
| $SnO_2$–CuO | Thin film | Sputtering | 20/150 | $8 \times 10^3$ | [25] |
| CuO–$SnO_2$ | Thin film | Pulsed laser deposition | 20/100 | $2.3 \times 10^3$ | [26] |
| CuO–$SnO_2$ nanowire | Thick film | Thermal evaporation | 20/300 | 809 | [27] |
| CuO–$SnO_2$ | Thick film | Precipitation/Impregnation and drop coating | 50/200 | 6.7 | [28] |
| 20 wt% CuO/$SnO_2$ | Thick film | Precipitation/Impregnation and spin coating | 10/200<br>10/150 | $1.359 \times 10^5$<br>$3.1 \times 10^4$ | This work |

vigorous agitation. The solution was then dropped onto 0.5 g of $SnO_2$ NPs with varying Cu concentrations from 5 to 25 wt%. Next, the suspension was continuously stirred until turning into homogeneous slurry and baked at 60 °C for 2 h in an oven. The resulting powders were annealed for 4 h at 300 °C at a heating rate of 10 °C/min.

The structural characteristics of NPs were evaluated using X-ray diffraction (XRD) with a Cu $K\alpha$ ($\lambda = 1.54056$ Å) X-ray source. The surface morphology and elemental distributions of NPs were examined using high-resolution scanning transmission electron microscopes (HR-TEM). The oxidation states of materials were studied using X-ray photoelectron spectroscopy (XPS) with an Al-$K_\alpha$ (1486.8 eV) X-ray source. The specific surface area of the NPs was measured using a nitrogen-adsorption analyser with Brunauer–Emmett–Teller analysis ($SSA_{BET}$).

### Fabrication and Characterization of Gas Sensor

To fabricate $SnO_2$ and 5–25 wt% $CuO/SnO_2$ sensors, 60 mg of powder was thoroughly mixed with an α-terpineol (Aldrich, 90%)-based vehicle containing ethyl cellulose (30–70 mPa s, Fluka) to produce a homogeneous paste. Next, a sensing film was deposited on an alumina substrate ($0.40 \times 0.55 \times 0.04$ cm$^3$) with prepatterned interdigitated gold electrodes (0.24 cm × 0.5 cm) by spin coating of the paste at 700 rpm for 10 s and at 3000 rpm for 30 s. The 200-nm-thick interdigitated Au electrodes were deposited on alumina substrates by a sputtering process with argon gas at a pressure of $3 \times 10^{-3}$ mbar. The interdigit spacing, width, and length were 100 μm, 100 μm, and 0.24 cm, respectively. The resulting sensors as illustrated in Fig. 1 were annealed for 2 h at 450 °C at a ramping rate of 4 °C/min to eliminate organic components from the sensing layers. The microstructures of sensing films were characterized using field-emission scanning electron microscopy (FE-SEM) and energy dispersive X-ray analysis (EDS).

### Gas Sensing Measurement

The sensor characteristics toward $H_2S$ in the concentration range of 0.15–10 ppm was measured in a home-made sealed stainless-steel test chamber with an active volume of 0.5 L (Fig. 1). An external Ni/Cr heater operated with a computer-controlled power supply was used to control the working temperature ranging from 150 to 350 °C. The selectivity properties were evaluated against $H_2$, $SO_2$, $CH_4$ and $C_2H_2$. At a given working temperature, the sensors were initially settled in synthetic dry air for 10 min to obtain a steady resistance in air. Next, the dry air was mixed with a target gas sample to a desired gas concentration at a fixed total flow rate (2 L/min) using computerized multichannel mass flow controllers (Brook Instruments model 5850E). Each gas sample was applied to the sensors for 25 min and the dry air was resumed for 45 min. The sensor resistance was measured by the amperometric method at a bias of 10 V DC using a picoammeter (Kiethley model 6487). The performances of sensors with various Cu concentrations were characterized in terms of gas response, response time, selectivity, and stability. The gas response ($S$) was expressed as $S = R_a/R_g$ for a reducing gas ($H_2S$, $H_2$, $CH_4$, $SO_2$ and $C_2H_2$), where $R_a$ and $R_g$ were the sensor resistance in air before and after exposure to a target gas, respectively. The response time ($t_{res}$) was the time taken to attain 90% of a steady-state response signal upon exposure to a target gas.

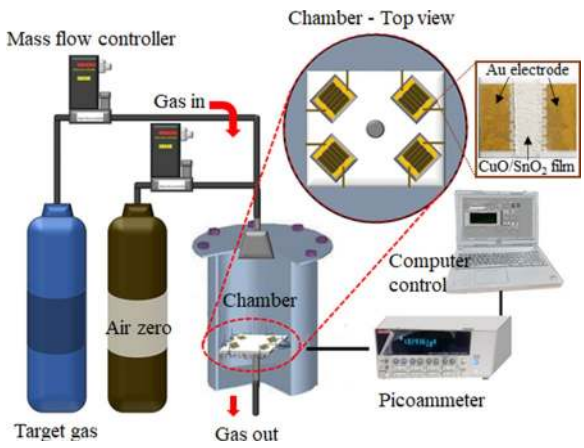


**Fig. 1** Gas-sensing measurement system with the photograph of a $CuO/SnO_2$ sensor

## Results and Discussion

### Structural Characteristics of Particles and Sensing Film

XRD patterns of CuO, $SnO_2$, and 5–25 wt% $CuO/SnO_2$ NPs are displayed in Fig. 2. The sharp diffraction peaks indicate the crystalline characteristic of all NPs. The diffraction patterns of $SnO_2$ and CuO correspond to tetragonal and monoclinic structures according to JCPDS files no 41-1445 and 45-0937, respectively. The $SnO_2$ powder exhibits three main peaks, while the CuO powder displays two distinct major peaks. The spectra for the 5–25 wt% $CuO/SnO_2$ NPs show the secondary CuO peaks of (002) and (111) planes together with the main $SnO_2$ peaks of (111), (101) and (211) planes, demonstrating the coexistence of CuO and $SnO_2$ phases. The mean crystallite sizes ($d$) of $CuO/SnO_2$ NPs were determined using Scherrer's equation ($d = K\lambda/(\beta\cos\theta)$ where $K$ is the geometric factor of 0.89 for spherical particles, $\lambda$ is the X-ray wavelength and $\beta$ is the full width at half maximum of an XRD peak at the angle,

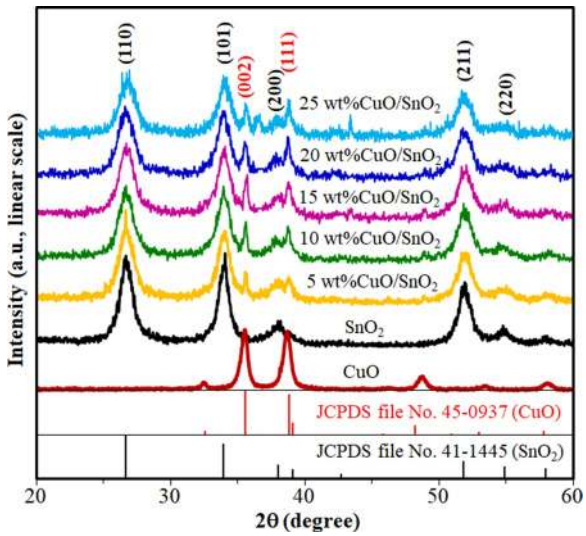


**Fig. 2** XRD pattern of CuO, $SnO_2$ and 5–25 wt% $CuO/SnO_2$ NPs

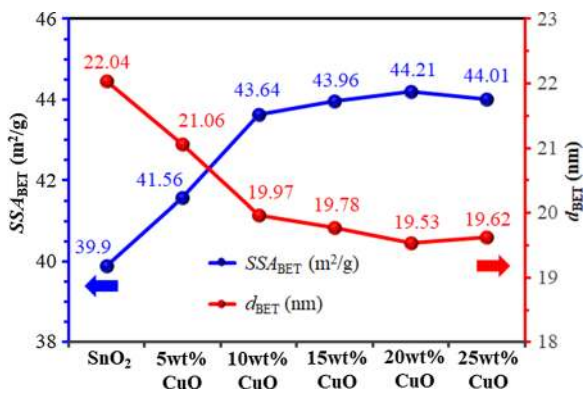


**Fig. 3** BET specific surface area ($SSA_{BET}$) and particle diameter ($d_{BET}$) of $SnO_2$ and 5–25 wt% $CuO/SnO_2$ NPs

$\theta$. The mean crystallite diameter of unloaded $SnO_2$ is estimated to be 10 nm, while that of 20 wt% $CuO/SnO_2$ NPs is relatively small at 7 nm. The result indicates the inhibition of grain growth due to CuO loading on $SnO_2$ NPs. The chemical compositions and oxidation states of CuO and SnO nanoparticles will be evaluated further by EDX and XPS analyses.

BET specific surface areas ($SSA_{BET}$) and particle diameters ($d_{BET}$) of $SnO_2$ and 5–25 wt% $CuO/SnO_2$ NPs are shown in Fig. 3. $SSA_{BET}$ of $CuO/SnO_2$ NPs substantially increases from 39.9 to 44.21 $m^2/g$, while the $d_{BET}$ reduces accordingly from 22.04 to 19.53 nm as the CuO content rises from 0 to 20 wt%. As the Cu content increases further to 25 wt%, $SSA_{BET}$ decreases slightly to 44.01 $m^2/g$ and $d_{BET}$ increases to 19.62 nm. The results agree with the XRD analysis of crystallite size. The influence of CuO loading level on $SSA_{BET}$ may be attribute to the inclusion of smaller CuO NPs produced by impregnation. The CuO NPs may act as separators to inhibit self-coagulation among $SnO_2$ NPs, resulting in the substantial increment of the effective surface area.

Figure 4 shows typical surface morphologies of coprecipitation/ impregnation synthesized $SnO_2$ and 20 wt% $CuO/SnO_2$ NPs. The BF-TEM images show that most $SnO_2$ particles exhibit spheroidal shapes with different diameters ranging from 5 to 20 nm. After CuO loading, the diameters of $SnO_2$ NPs tend to be smaller but the secondary phase of CuO cannot be clearly identified (Fig. 4d–f). The related SAED patterns display dotted ring features of polycrystalline tetragonal $SnO_2$ structures with main diffraction rings corresponding to (110), (101), (200), (211) and (112) planes of $SnO_2$ as well as (002) plane of CuO in agreement the XRD analysis. The rings related to CuO were quite obscure due likely to weak diffraction signal from very small CuO secondary phase. Correspondingly, the HR-TEM images show lattice fringes on nanoparticles mainly associated with the planes of $SnO_2$ crystals. The secondary CuO phase structures cannot be observed in HR-TEM image due possibly to their very small sizes beyond the resolution of the TEM instrument.

Scanning transmission electron microscopy (STEM) and high-resolution EDS mapping analysis were employed to investigate the distributions of CuO in 20 wt% $CuO/SnO_2$ NPs as presented in Fig. 5. The STEM image illustrates a cluster of roughly round nanoparticles with diameters in the range of 5–15 nm in agreement with the TEM images but with relatively low image resolution due to scanning aberration. The corresponding EDS maps of Sn, O, and Cu elements demonstrate the detailed distribution of these species on various $SnO_2$ nanoparticles in the selected area. Apparently, Cu species are widely distributed on particles with similar density to Sn and O species. The results suggest that the CuO secondary nanoparticles are present and closely distributed on $SnO_2$ surfaces forming distributed CuO–$SnO_2$ junctions within the $CuO/SnO_2$ composite. However, the particles and related junctions are very small at molecular scales so that they cannot be exactly discerned by the TEM/STEM characterizations.

Figure 6 illustrates the cross-sectional morphologies and chemical compositions of $SnO_2$ and 20 wt% $CuO/SnO_2$ films. Both layers are approximately 20 μm thick and similarly comprise agglomerated particles on solid-textured substrates. The elemental compositions of $SnO_2$, and 20 wt% $CuO/SnO_2$ are listed in the inset tables of Fig. 5b, d. It reveals that the atomic contents of Sn and O of $SnO_2$ NPs are lower than the expected values (33:67)

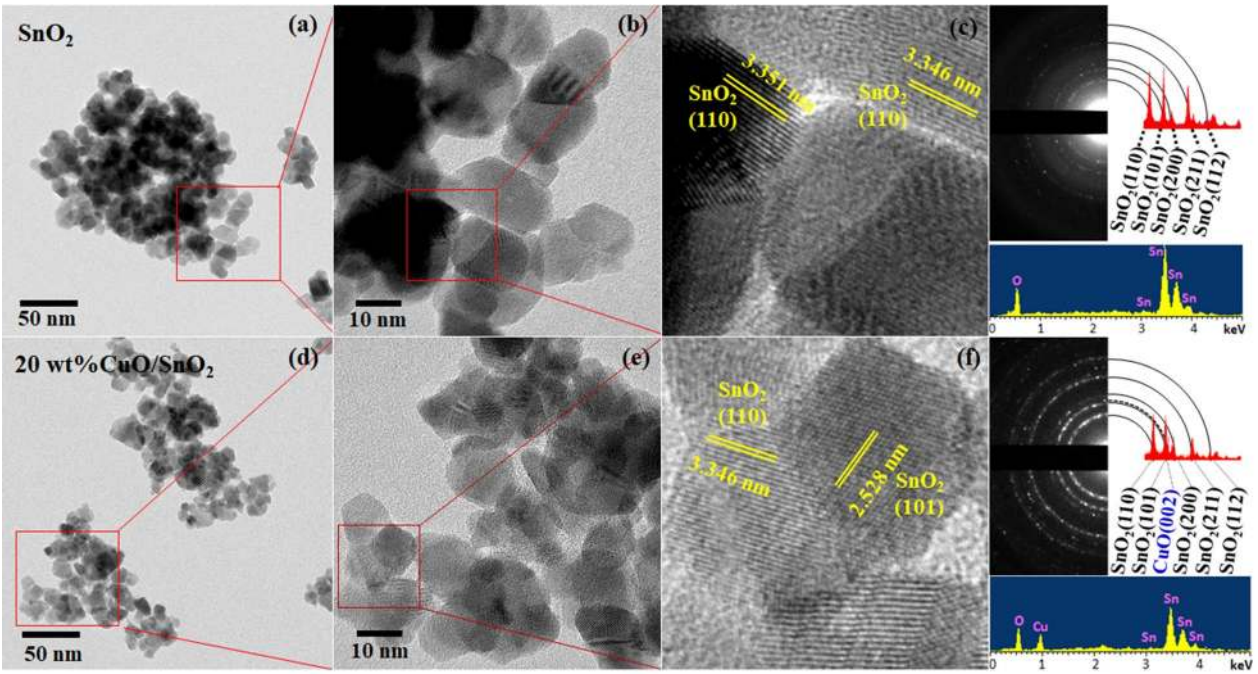


**Fig. 4** BF-TEM and HR-TEM images with corresponding SAED patterns of **a**–**c** $SnO_2$ NPs and **d**–**f** 20 wt% $CuO/SnO_2$ NPs

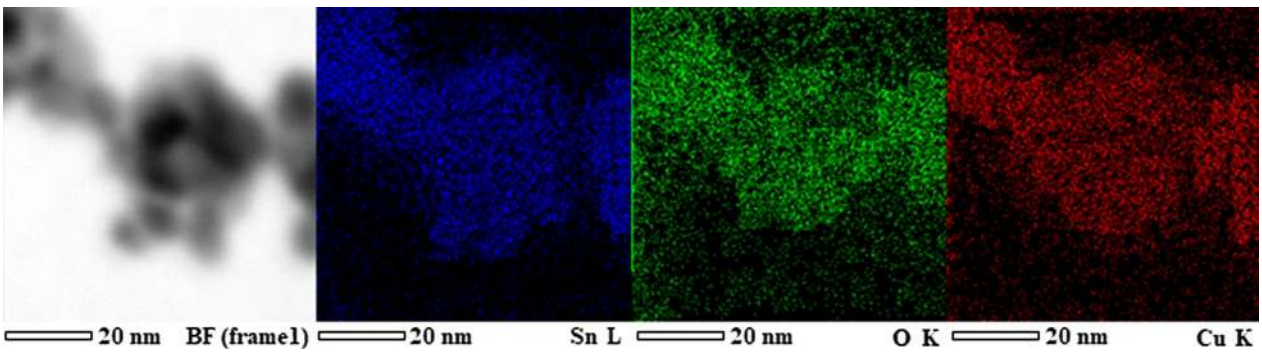


**Fig. 5** Scanning-TEM (STEM) image and corresponding elemental EDS maps of 20 wt% $CuO/SnO_2$ NPs

of stoichiometric $SnO_2$. With 20 wt% CuO loading, a Cu peak appears with a high Cu content of ~ 15.6 wt% or 7.04 at%, which is still smaller than that of Sn. Additionally, the Cu content from five different areas is found to vary from 14 to 18 wt%, indicating some variation of chemical composition within the film. Therefore, CuO loading by impregnation does not markedly influence particle morphologies but considerably changes the elemental composition.

Figure 7 presents the oxidation states of elements in $SnO_2$ and 20 wt% $CuO/SnO_2$ NPs. The XPS survey spectrum of $SnO_2$ reveals the presence of C, O and Sn, while that of 20 wt% $CuO/SnO_2$ demonstrates the existence of C, O, Sn and Cu. The results confirm the formation of $CuO/SnO_2$ composites with typical organic/carbon contaminations on surfaces. For Sn element, the $Sn3d_{5/2}$ and $Sn3d_{3/2}$ doublet peaks of $SnO_2$ and 20 wt% $CuO/SnO_2$ NPs are similarly observed at the binding energies of 486.8–487.1 eV and 495.2–495.5 eV, respectively. The peak locations can be assigned to the $Sn^{4+}$ oxidation state of $SnO_2$ [29]. In the case of 20 wt% $CuO/SnO_2$ NPs, the Cu2p core levels comprise $Cu2p^{3/2}$ and $Cu2p^{1/2}$ peaks centred at 933.5 eV and 953.4 eV along with the satellite peaks at ~ 942.9 and ~ 964.2 eV, corresponding to the $Cu^{2+}$ oxidation state of CuO [30]. The observed oxidation states affirm the coexistence of CuO and $SnO_2$ structures.

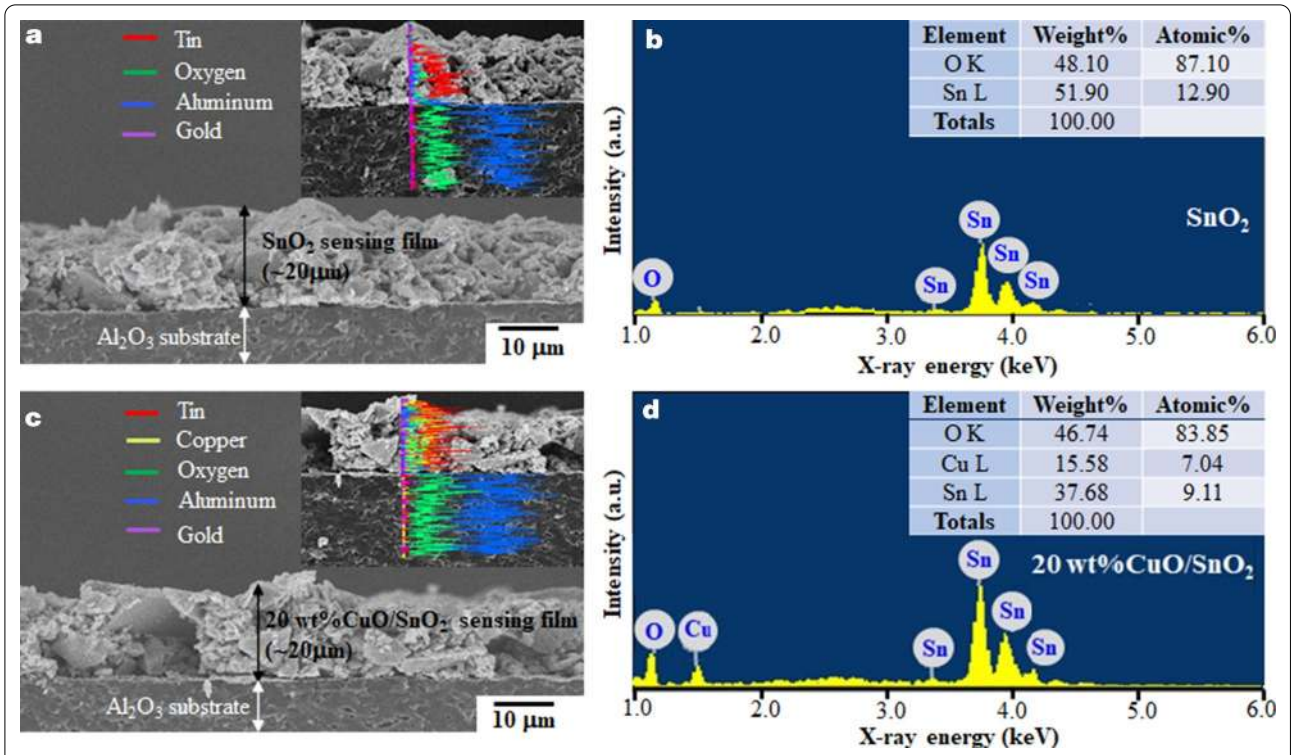


**Fig. 6** Cross-sectional FE-SEM images with EDS line-scan profiles (inset) and corresponding EDS spectra with elemental composition tables (inset) of the **a**, **b** $SnO_2$, and **c**, **d** 20 wt%CuO/$SnO_2$ NPs sensing films

### Gas-Sensing Characteristics

Figure 8a displays the changes in resistance of CuO, $SnO_2$ and 5–25 wt% CuO/$SnO_2$ films subjected to $H_2S$ pulses with varying concentrations from 0.15 to 10 ppm at a working temperature of 200 °C. The resistance in air of $SnO_2$ film increases by more than two orders of magnitude after loading CuO with 5–25 wt% contents. Additionally, it is observed that the baseline resistances of various CuO/$SnO_2$ sensors are not very different and only tend to increase slightly with increasing CuO loading level. To identify whether the resistance is changed due to the film geometry or material related properties, the film resistivity was additionally measured by the well-known four-probe method using 4-stripe Au/Cr electrodes with an interelectrode spacing of 100 μm and a bias current of 0.1 μA. The measured average resistivity values of CuO, $SnO_2$, and 5–25 wt% CuO/$SnO_2$ films in air at 350 °C are ~ $8.1 \times 10^3$, $2.1 \times 10^4$ and $7.4 \times 10^7 - 1.8 \times 10^8$ Ω cm, respectively. The results confirm significant differences in resistivity among the three sets of materials and the similarities in resistivity among 5–25 wt% CuO/$SnO_2$ films. This behavior may be explained based on two effects including the percolation breaking of aggregated $SnO_2$ nanoparticles due to CuO secondary nanoparticles and the formation of CuO/$SnO_2$ (p–n) heterojunctions. The TEM/HR-TEM/STEM data suggest that CuO secondary nanoparticles may be formed surrounding the $SnO_2$ nanoparticles, thus breaking the percolation of agglomerated $SnO_2$ particles and forcing most conduction paths to be across the CuO nanoparticles. In addition, the formation of CuO/$SnO_2$ heterojunctions may induce carrier depletion regions throughout secondary CuO nanoparticles due to the work function difference, creating highly resistive conduction paths. Thus, an addition of CuO to $SnO_2$ particles at the level above the minimum value required to break the percolation of $SnO_2$ particles will cause a large increase of resistance as fully depleted CuO particles block electrical conduction. The lowest Cu content in this study of 5% is quite substantial and thus likely to exceed the percolation breaking threshold. Further addition of CuO will only slightly increase the resistance since the electrical conduction via fully depleted CuO is already nearly minimal. Other effects including particle/grain sizes, film thickness, electrode separation, and electrode contact may be neglected since they are not greatly changed according to the structural characterization results. Upon exposure to $H_2S$, the sensor resistances decrease rapidly before recovering to the baseline levels after the resumption of dry air, confirming a typical n-type sensing characteristic. Interestingly, the baseline

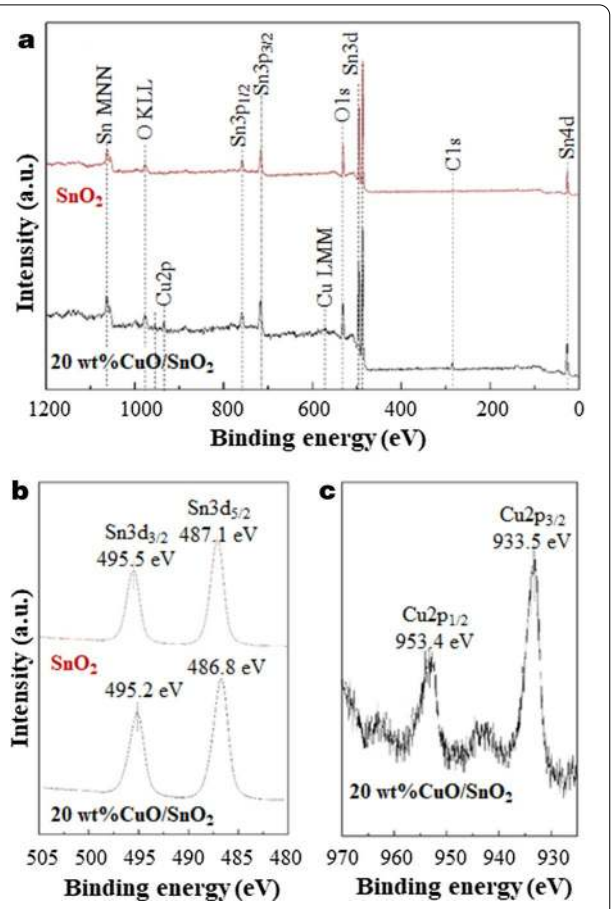


**Fig. 7** **a** Survey and high-resolution XPS spectra of the **b** Sn3d and **c** Cu 2*p* core levels of $SnO_2$ and 20 wt% $CuO/SnO_2$ NPs

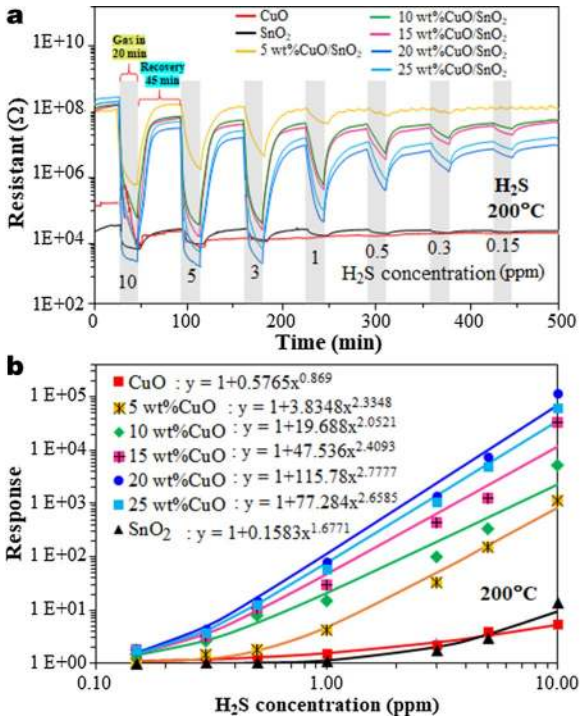


**Fig. 8** **a** Dynamic response of CuO, $SnO_2$ and 5–25 wt%$CuO/SnO_2$ gas sensors subjected to 0.15 to 10 ppm $H_2S$ pulses at 200 °C and **b** corresponding sensor response vs. $H_2S$ concentration

resistance of CuO sensor considerably drifts downward after several $H_2S$ pulses in contrast to the $SnO_2$ sensor that shows insignificant baseline drift. In the case of $CuO/SnO_2$ sensors, the baseline drift tends to increase with increasing Cu content. These behaviors may be related to the slow and incomplete CuO–CuS transformative reactions to be further discussed in Sect. 3.3.

The corresponding sensor response plotted versus $H_2S$ concentration at 200 °C is shown in Fig. 8b. All sensor responses increase monotonically with increasing $H_2S$ concentration. The response characteristics of all sensors conform well to the power law according to the equations as displayed along with the inset labels in Fig. 8b. The power-law exponent of CuO is close to 1, while that of $SnO_2$ sensors is around 1.5 and those of CuO-loaded $SnO_2$ sensors are larger than 2, suggesting differences in $H_2S$ reaction mechanisms on the surfaces of these materials [31]. Furthermore, the sensor response increases greatly as the CuO content increases from 0 to 20 wt% before slightly declining at a higher CuO content of 25 wt% and the 20 wt% $CuO/SnO_2$ sensor offers the highest response of $1.36 \times 10^5$ to 10 ppm $H_2S$ at 200 °C. Moreover, it exhibits decent responses of ~ 2, 5, 20 and 230 at the lower $H_2S$ concentrations of 0.15, 0.3, 0.5 and 1 ppm, respectively. The excellent performances of 20 wt% $CuO/SnO_2$ sensor may be attributed to the increase of specific surface area due to CuO loading and the formation of $CuO/SnO_2$ heterojunctions to be further discussed in the next section.

Figure 9 presents the plot of the response versus working temperature of unloaded and CuO-loaded $SnO_2$ sensors at a $H_2S$ concentration of 10 ppm. The $H_2S$ responses of $CuO/SnO_2$ NPs sensors increase significantly with the increasing temperature from 150 to 200 °C and then reduce rapidly when the temperature further rises. Hence, 200 °C is the optimal working temperature of the CuO-loaded $SnO_2$ sensors. Specifically, the optimal 20 wt% $CuO/SnO_2$ sensor gives the highest response of $1.36 \times 10^5$, which is much higher than those of other sensors at 200 °C. The optimal working temperature of 200 °C corresponds to the temperature that maximizes the $H_2S$ adsorption rate relative to desorption rate of $CuO/SnO_2$ surfaces. Furthermore, 5–25 wt% $CuO/SnO_2$ sensors display a lower optimal working temperature than that of $SnO_2$ sensor (250 °C). The relatively low

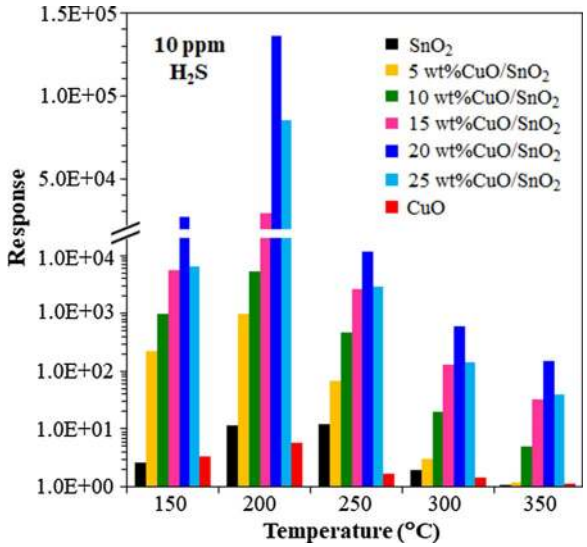


**Fig. 9** Effect of working temperature on response to 10 ppm $H_2S$ of CuO, $SnO_2$ and 5–25 wt%CuO/$SnO_2$ sensors

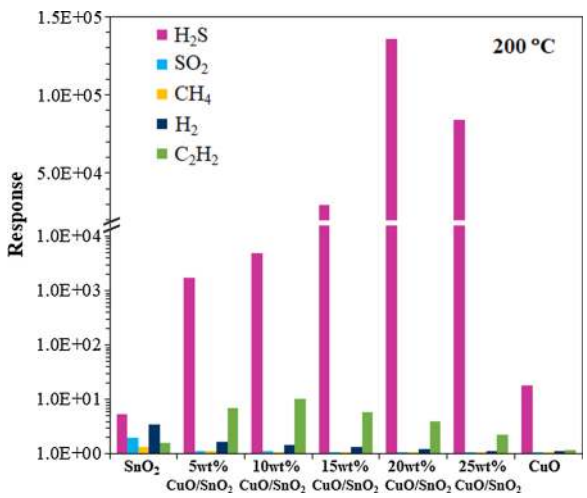


**Fig. 10** Responses of CuO, $SnO_2$ and 5–25 wt%CuO/$SnO_2$ sensors toward $H_2S$ (10 ppm), $SO_2$ (200 ppm), $CH_4$ (1000 ppm), $H_2$ (1000 ppm) and $C_2H_2$ (1000 ppm) at 200 °C

optimal working temperature will be subsequently explicated by CuO loading effects.

Figure 10 summarizes the $H_2S$ selectivity of 0–25 wt% CuO/$SnO_2$ sensors against $SO_2$, $H_2$, $CH_4$ and $C_2H_2$. This type of sensor exhibits the highest $H_2S$ selectivity, i.e., more than three orders of magnitude higher $H_2S$ response than those of other gases. The data prove that CuO is the catalyst that selectively accelerates the reaction with $H_2S$. The selectivity behavior may also be attributed to the increase of active sites for $H_2S$ adsorption due to the highest specific surface area of 20 wt% CuO/$SnO_2$ NPs. The enhancements for other tested gases are not significant due probably to relatively weak interactions between gas molecules and 20 wt% CuO/$SnO_2$ NPs. The attained $H_2S$ responses of 20 wt% CuO/$SnO_2$ sensors are substantially better than those of many other metal-loaded $SnO_2$ and CuO-loaded $SnO_2$ sensors made by distinct techniques as listed in Table 1. However, the achieved optimal working temperature of 200 °C is higher than the values of some reports at 100–150 °C. The lower working temperature is generally preferred in practical applications. Nevertheless, the 20 wt% CuO/$SnO_2$ sensor may operate at a lower working temperature of 150 °C where the sensor still exhibits a high response of $3.1 \times 10^4$ to 10 ppm $H_2S$ (Fig. 9), which is also higher than the response values of other sensors reported in Table 1. Therefore, the CuO-loaded $SnO_2$ sensor is a highly promising candidate for $H_2S$ sensing due to its high $H_2S$ response, high $H_2S$ selectivity and low working temperature.

Finally, the stability, repeatability, and reproducibility of CuO/$SnO_2$ sensors were evaluated from four samples produced in the same batch. All sensors exhibited good stability with less than 15% drift in sensor response over 1 month under the same operating conditions. Moreover, each sensor showed good repeatability with less than 12% response variation from 8 repeated measurements. In addition, four sensors from the same batch were found to have fair response variation of less than 26% evaluated under the same test condition.

### Gas-Sensing Mechanisms

The characterization results suggest the formation of CuO/$SnO_2$ composite comprising very small CuO species on $SnO_2$ nanoparticles. Thus, the mechanisms for electrical response of CuO/$SnO_2$ sensing films toward $H_2S$ may be described based on the composite junction theory of p-n junctions at the contacts between p-type CuO and n-type $SnO_2$ as depicted in Fig. 11. For undoped $SnO_2$, chemisorbed oxygen species ($O^-$) are formed resulting in the creation of depletion regions on surface at a moderate temperature. Upon exposure to $H_2S$, $H_2S$ molecules interact with adsorbed oxygen species on $SnO_2$ surface ($H_2S + 3O^- \rightarrow H_2O + SO_2 + e^-$), releasing electrons to $SnO_2$ conduction band and reducing the sensor resistance. At a low working temperature of 200 °C, the concentration of oxygen species is very low, leading to a low reaction rate and a low $H_2S$ response. With CuO loading, additional depletion regions will be formed at various p-n junctions around the surface of $SnO_2$ nanoparticles. In addition, carriers in secondary CuO nanoparticles, which can break percolation of aggregated $SnO_2$ nanoparticles, may be fully depleted, resulting in a high electrical resistance in air. In ambient with $H_2S$, the gas molecules can

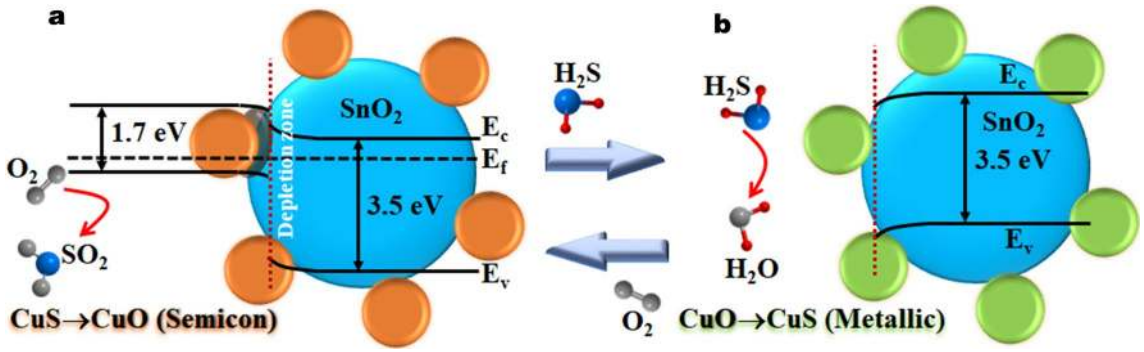


**Fig. 11** Energy band diagrams of $CuO/SnO_2$ heterojunctions **a** before and **b** after exposure to $H_2S$ ($E_f$ = Fermi-energy level, $E_C$ = conduction band and $E_V$ = valence band)

additionally react with the catalytic CuO NPs, leading to the creation of copper sulfide (CuS) via the reaction (Eq. 1) [26]:

$$CuO + H_2S \rightarrow CuS + H_2O \quad (1)$$

CuS is more conductive than CuO, leading to lower potential barriers at depletion regions around the interfaces. The induction of metallic CuS is equivalent to the injection of free electrons into the p-type material (CuO), making it less p-type. This encourages the electron transfer from CuS to $SnO_2$, resulting in additional decrease of depletion width and increase of the electrical conductance of $SnO_2$. The decrease of resistance due to the formation of CuS is much larger than the reduction due to the reducing reaction with oxygen species due to transfer of more electrons from CuS. At low CuO contents, there are relatively few and small CuO nanoparticles that are fully transformed into CuS surrounding $SnO_2$ particles. It will provide a limited amount of electrons to $SnO_2$ due to relatively few heterojunctions, resulting in small reduction of depletion region widths in $SnO_2$ and small resistance drop upon $H_2S$ exposure. As the CuO content increases, the numbers of transformed CuS nanoparticles and heterojunctions increase, leading to an increased number of conduction paths through CuS as well as much reduced $SnO_2$ depletion region widths and thus a higher resistance drop that can be achieved after $H_2S$ exposure. However, CuO particles may coalesce into large ones and the number of $CuO/SnO_2$ heterojunctions becomes lower at very high CuO content (> 20 wt%). The large CuO particles will not be fully transformed to CuS due to limited reaction depth with $H_2S$ and the depletion regions in CuO cores remain, limiting the conduction through CuO and reducing attainable resistance drop. In the case of CuO, the response is low despite the formation of CuS because the resistance of CuO is already low and is not much higher than that of CuS [20]. After $H_2S$ in atmosphere extinguishes, the electrical resistance returns to its original values as CuS can be reoxidized to CuO in air at an elevated temperature according to the reaction (Eq. 2) [26]:

$$CuS + O_2 \rightarrow CuO + SO_2 \quad (2)$$

The oxidation of CuS is slow at a low working temperature. As the increase of working temperature, the oxidation rate increases and lead to the increase of recovery rate. Since the CuS–CuO transformative reaction (Eq. (2)) is slower than the CuO–CuS one (Eq. (1)) at this working temperature, residual CuS materials can remain after subjecting CuO to several $H_2S$ pulses. This results in a substantial downward baseline drift of CuO sensor and the increase of baseline drift with increasing Cu content of $CuO/SnO_2$ sensors as previously observed in Fig. 8a. However, there is an exception in the case of 5 wt% $CuO/SnO_2$ sensor, which exhibits a small upward drift of baseline resistance after the first pulse. It may occur because the sensor did not fully reach the steady state before applying the first pulse leading to some upward recovery owing to oxidation in air while the drift due to CuS–CuO transformation at this low Cu content is relatively small due to a low residual CuS content. At higher Cu contents, the downward drifts due to residual CuS are large and overwhelm the small upward recovery. The baseline drift considerably reduces the validity, repeatability and stability of sensor response of $CuO/SnO_2$ as the response to a subsequent $H_2S$ pulse is affected by the residual CuS concentration after the previous $H_2S$ exposure leading to negative deviations from the ideal response behavior. Thus, the calculated responses of the $CuO/SnO_2$ sensors especially with high Cu contents in Fig. 8b are lower the theoretical values under no residual CuS condition. The problems can be reduced by increasing the working temperature. Thus, the sensors may operate above

the optimal working temperature at 250 °C when the drift is low, and response is still high. CuS structure can be formed at 103 °C and will be transformed into $Cu_2S$, a less conductive ionic conductor, at the temperature above 220 °C [26]. Consequently, the sensor response of $CuO/SnO_2$ NPs decreases when the temperature rises above 200 °C. The observed high $H_2S$ selectivity against $SO_2$, $H_2$, $CH_4$ and $C_2H_2$ can also be explained in relation to the working temperature. At the optimal working temperature of 200 °C, the rate of CuO–CuS transformation is high, while the reducing reaction rates of $SO_2$, $H_2$, $CH_4$ and $C_2H_2$ are very low because these reactions require the chemisorbed oxygen species whose density is still very low at this working temperature.

## Conclusions

0–25 wt% $CuO/SnO_2$ NPs were fabricated using the precipitation and impregnation method. XRD, BET, TEM, SEM, EDS and XPS data suggested the loading of very small CuO nanoparticles on larger $SnO_2$ NPs. The gas-sensing results demonstrated that CuO loading greatly enhanced the $H_2S$ response of $SnO_2$ NPs with an optimal Cu content of 20 wt%. The 20 wt%$CuO/SnO_2$ sensor can perceive low-ppm $H_2S$ concentrations with ultra-high responses ($1.4 \times 10^5$ at 10 ppm), short response times (35 s), fair recovery times (a few minutes), very high $H_2S$ selectivity against $SO_2$, $CH_4$, $H_2$ and $C_2H_2$ and good stability. They could also offer a wide detection range (0.15–10 ppm) when compared with the unloaded one (3–10 ppm). Therefore, the $CuO/SnO_2$ sensors synthesized by precipitation and impregnation could be a promising candidate for $H_2S$ detection in environmental applications.

#### Abbreviations

NPs: Nanoparticles; XRD: X-ray diffraction; HR-TEM: High-resolution transmission electron microscopy; FE-SEM: Field-emission scanning electron microscopy; EDX: Energy-dispersive X-ray spectroscopy; AFM: Atomic force microscopy; BET: Brunauer–Emmett–Teller; $SSA_{BET}$: Specific surface area; XPS: X-ray photoelectron spectroscopy.

#### Acknowledgments

The authors are grateful for the financial support from Thailand Graduate Institute of Science and Technology (TGIST), National Science and Technology Development Agency (NSTDA), National Research Council of Thailand (NRCT), Nanoscience and Nanotechnology Program, Applied Chemistry Program, Applied Physics Program, Faculty of Science, Maejo University, Thailand. We also wish to thank Center of Excellence in Materials Science and Technology, Chiang Mai University for the chemical materials and other technical assistance under the administration of Materials Science Research Center, Faculty of Science, Chiang Mai University. Special thanks are given to National Electronics and Computer Technology Center, Pathum Thani, Thailand for the sensor facility and other technical assistance. The authors also would like to acknowledge the BL5.3:SUT-NANOTEC-SLRI XPS, Synchrotron Light Research Institute (SLRI), Thailand for the XPS measurement. Additionally, the authors gratefully acknowledge the Thailand Research Fund for TRF Research Team Promotion Grant (RTA6180004).

#### Authors' contributions

V.K and P.L carried out the experiments, acquired the original data, participated in the sequence alignment, fabricated the devices, performed measurements and wrote the manuscript. A.W, A.T and S.P assisted in processing the data and figures. K.J and N.C helped measure the devices. All the authors read and approved the final manuscript.

#### Funding

The authors acknowledge the financial support from the National Research Council of Thailand (NRCT) and Faculty of Science, Maejo University.

#### Availability of data and materials

The datasets supporting the conclusions of this article are included in the article.

## Declarations

#### Competing interests

The authors declare that they have no competing interests.

#### Author details

[1]Applied Chemistry Program, Faculty of Science, Maejo University, Chiang Mai 50290, Thailand. [2]Nanoscience and Nanotechnology Program, Faculty of Science, Maejo University, Chiang Mai 50290, Thailand. [3]Applied Physics Program, Faculty of Science, Maejo University, Chiang Mai 50290, Thailand. [4]National Security and Dual-Use Technology Center, National Science and Technology Development Agency, Klong Luang, Phathumthani 12120, Thailand. [5]Opto-Electrochemical Sensing Research Team (OEC), National Electronics and Computer Technology Center (NECTEC), Pathumthani 12120, Thailand. [6]Synchrotron Light Research Institute, Nakhon Ratchasima 30000, Thailand. [7]Center of Advanced Materials for Printed Electronics and Sensors, Materials Science Research Center, Faculty of Science, Chiang Mai University, Chiang Mai 50200, Thailand.

Received: 20 July 2020 Accepted: 18 April 2021
Published online: 28 April 2021

#### References

1. Kim H, Jin C, Park S, Kim S, Lee C (2012) $H_2S$ gas sensing properties of bare and Pd-functionalized CuO nanorods. Sens Actuators B 161:594–599
2. Guo W, Liu T, Zhang H, Sun R, Chen Y, Zeng W, Wang Z (2012) Gas-sensing performance enhancement in ZnO nanostructures by hierarchical morphology. sens actuators b 166–167:492–499
3. Sun R, Wang Z, Saito M, Shibata N, Ikuhara Y (2015) Atomistic mechanisms of nonstoichiometry-induced twin boundary structural transformation in titanium dioxide. Nat Commun 6:1–7
4. Wang J, Zeng W, Wang Z (2016) Assembly of 2D nanosheets into 3D flower-like NiO: synthesis and the influence of petal thickness on gas-sensing properties. Ceram Int 42:4567–4573
5. Guo W, Fu M, Zhai C, Wang Z (2014) Hydrothermal synthesis and gas-sensing properties of ultrathin hexagonal ZnO nanosheets. Ceram Int 40:2295–2298
6. Zeng W, Liu T, Wang Z, Tsukimoto S, Saito M, Ikuhara Y (2009) Selective detection of formaldehyde gas using a Cd-doped $TiO_2$–$SnO_2$ sensor. Sensors 9:9029–9038
7. Song Z, Xu S, Li M, Zhang W, Yu H, Wang Y, Liu H (2016) Solution-processed $SnO_2$ nanowires for sensitive and fast-response $H_2S$ detection. Thin Solid Films 618:232–237
8. Luo W, Deng J, Fu Q, Zhou D, Hu Y, Gong S, Zheng Z (2015) Nanocrystalline $SnO_2$ film prepared by the aqueous sol–gel method and its application as sensing films of the resistance and SAW $H_2S$ sensor. Sens Actuators B 217:119–128
9. Nakla W, Wisitsora-at A, Tuantranont A, Singjai P, Phanichphant S, Liewhiran C (2014) $H_2S$ sensor based on $SnO_2$ nanostructured film prepared by high current heating. Sens Actuators B 203:565–578
10. Kolhe PS, Koinkar PM, Maiti N, Sonawane KM (2017) Synthesis of Ag doped $SnO_2$ thin films for the evaluation of $H_2S$ gas sensing properties. Physica B: Con Mat 524:90–96

11. Sukunta J, Wisitsoraat A, Tuantranont A, Phanichphant S, Liewhiran C (2017) Highly-sensitive $H_2S$ sensors based on flame-made V-substituted $SnO_2$ sensing films. Sens Actuators B 242:1095–1107
12. Kabcum S, Tammanoon N, Wisitsoraat A, Tuantranont A, Phanichphant S, Liewhiran C (2016) Role of molybdenum substitutional dopants on $H_2S$-sensing enhancement of flame-spray-made $SnO_2$ nanoparticulate thick films. Sens Actuators B 235:678–690
13. Ma J, Liu Y, Zhang H, Ai P, Gong N, Wu Y, Yu D (2015) Room temperature ppb level $H_2S$ detection of a single Sb-doped $SnO_2$ nanoribbon device. Sens Actuators B 216:72–79
14. Ramgir NS, Datta N, Kumar S, Kailasaganapathi S, Patil UV, Karmakar N, Kaur M, Debnath AK, Kothari DC, Aswal DK, Gupta SK (2015) Effect of Fe modification on $H_2S$ sensing properties of rheotaxially grown and thermally oxidized $SnO_2$ thin films. Mater Chem Phys 156:227–237
15. Liu J, Lu Y, Cui X, Geng Y, Jin G, Zhai Z (2017) Gas-sensing properties and sensitivity promoting mechanism of Cu-added $SnO_2$ thin films deposited by ultrasonic spray pyrolysis. Sens Actuators B 248:862–867
16. Wang C, Zeng W, Luo L, Zhang P, Wang Z (2016) Gas-sensing properties and mechanisms of Cu-doped $SnO_2$ spheres towards $H_2S$. Ceram Int 42:10006–10013
17. Kumar V, Sen S, Muthe KP, Gaur NK, Gupta SK, Yakhmi JV (2009) Copper doped $SnO_2$ nanowires as highly sensitive $H_2S$ gas sensor. Sens Actuators B 138:587–590
18. Ghimbeu CM, Lumbreras M, Siadat M, Landschoot RC, Schoonman J (2008) Electrostatic sprayed $SnO_2$ and Cu-doped $SnO_2$ films for $H_2S$ detection. Sens Actuators B 133:694–698
19. Toan NV, Deng J, Fu Q, Zhou D, Hu Y, Gong S, Zheng Z (2015) Scalable fabrication of $SnO_2$ thin films sensitized with CuO islands for enhanced $H_2S$ gas sensing performance. Appl Surf Sci 324:280–285
20. Choi KI, Kim HJ, Kang YC, Lee J-H (2014) Ultraselective and ultrasensitive detection of $H_2S$ in highly humid atmosphere using CuO-loaded $SnO_2$ hollow spheres for real time diagnosis of halitosis. Sens Actuators B 194:371–376
21. Shao F, Hoffmanna MWG, Prades JD, Zamani R, Arbiol J, Morante JR, Varechkina E, Rumyantseva M, Gaskov A, Giebelhaus I, Fischer T, Mathur S, Hernández-Ramírez F (2013) Heterostructured p-CuO (nanoparticle)/n-$SnO_2$ (nanowire) devices for selective $H_2S$ detection. Sens Actuators B 181:130–135
22. Verma MK, Gupta V (2012) A highly sensitive $SnO_2$–CuO multilayered sensor structure for detection of $H_2S$ gas. Sens Actuators B 166–167:378–385
23. Choi SW, Zhang J, Akash K, Kim SS (2012) $H_2S$ sensing performance of electrospun CuO-loaded $SnO_2$ nanofibers. Sens Actuators B 169:54–60
24. Zhao Y, He X, Li J, Gao X, Jia J (2012) Porous CuO/$SnO_2$ composite nanofibers fabricated by electrospinning and their $H_2S$ sensing properties. Sens Actuators B 165:82–87
25. Chowdhuri A, Singh SK, Sreenivas K, Gupta V (2010) Contribution of adsorbed oxygen and interfacial space charge for enhanced response of $SnO_2$ sensors having CuO catalyst for $H_2S$ gas. Sens Actuators B 145:155–166
26. Verma M, Chowdhuri A, Sreenivas K, Gupta V (2010) Comparison of $H_2S$ sensing response of hetero-structure sensor (CuO–$SnO_2$) prepared by rf sputtering and pulsed laser deposition. Thin Solid Films 518:181–182
27. Hwang IS, Choi JK, Kim SJ, Dong KY, Kwon JH, Jub BK, Lee JH (2009) Enhanced $H_2S$ sensing characteristics of $SnO_2$ nanowires functionalized with CuO. Sens Actuators B 142:105–110
28. Liu J, Huang X, Ye G, Liu W, Jiao Z, Chao W, Zhou Z, Yu Z (2003) $H_2S$ Detection sensing characteristic of CuO/$SnO_2$ sensor. Sensors 3:110–118
29. Zhang Z, Xu M, Liu L, Ruan X, Yan J, Zhao W, Yun J, Wang Y, Qin S, Zhang T (2018) Novel $SnO_2$@ZnO hierarchical nanostructures for highly sensitive and selective $NO_2$ gas sensing. Sens Actuators B 257:714–727
30. Wang Y, Qu F, Liu J, Wang Y, Zhou J, Ruan S (2015) Enhanced $H_2S$ sensing characteristics of CuO–NiO core-shell microspheres sensors. Sens Actuators B 209:515–523
31. Yamazoe N, Shimanoe K (2008) Theory of power laws for semiconductor gas sensors. Sens Actuators B Chem 128:566–573


## Publisher's Note